



Article

Investigation of the Spin Crossover Properties of Three Dinuclear Fe(II) Triple Helicates by Variation of the Steric Nature of the Ligand Type

Alexander R. Craze¹, Natasha F. Sciortino², Mohan M. Badbhade³, Cameron J. Kepert², Christopher E. Marjo³ and Feng Li^{1,*}

¹ School of Science and Health, Western Sydney University, Locked Bag 1797, Penrith, Sydney, NSW 2751, Australia; 17717986@student.westernsydney.edu.au

² School of Chemistry, University of Sydney, Sydney, NSW 2006, Australia; natasha.sciortino@sydney.edu.au (N.F.S.); cameron.kepert@sydney.edu.au (C.J.K.)

³ Mark Wainwright Analytical Centre, University of New South Wales, Sydney, NSW 2052, Australia; m.badbhade@unsw.edu.au (M.M.B.); c.marjo@unsw.edu.au (C.E.M.)

* Correspondence: Feng.Li@westernsydney.edu.au; Tel.: +61-2-9685-9987

Received: 14 August 2017; Accepted: 13 September 2017; Published: 21 September 2017

Abstract: The investigation of new spin-crossover (SCO) compounds plays an important role in understanding the key design factors involved, informing the synthesis of materials for future applications in electronic and sensing devices. In this report, three bis-bidentate ligands were synthesized by Schiff base condensation of imidazole-4-carbaldehyde with 4,4-diaminodiphenylmethane (**L**¹), 4,4'-diaminodiphenyl sulfide (**L**²) and 4,4'-diaminodiphenyl ether (**L**³) respectively. Their dinuclear Fe(II) triple helicates were obtained by complexation with Fe(BF₄)₂·6H₂O in acetonitrile. The aim of this study was to examine the influence of the steric nature of the ligand central atom (–X–, where X = CH₂, S or O) on the spin-crossover profile of the compound. The magnetic behaviours of these compounds were investigated and subsequently correlated to the structural information from single-crystal X-ray crystallographic experiments. All compounds [Fe₂(**L**¹)₃](BF₄)₂ (**1**), [Fe₂(**L**²)₃](BF₄)₂ (**2**) and [Fe₂(**L**³)₃](BF₄)₂ (**3**), demonstrated approximately half-spin transitions, with *T*_{1/2↓} values of 155, 115 and 150 K respectively, corresponding to one high-spin (HS) and one low-spin (LS) Fe(II) centre in a [LS–HS] state at 50 K. This was also confirmed by crystallographic studies, for example, bond lengths and the octahedral distortion parameter (Σ) at 100 K. The three-dimensional arrangement of the HS and LS Fe(II) centres throughout the crystal lattice was different for the three compounds, and differing extents of intermolecular interactions between BF₄[–] counter ions and imidazole N–H were present. The three compounds displayed similar spin-transition profiles, with **2** (–S–) possessing the steepest nature. The shape of the spin transition can be altered in this manner, and this is likely due to the subtle effects that the steric nature of the central atom has on the crystal packing (and thus inter-helical Fe–Fe separation), intermolecular interactions and Fe–Fe intra-helical separations.

Keywords: spin-crossover; triple helicate; dinuclear; Fe(II) complex

1. Introduction

The design of new spin-crossover (SCO) coordination complexes is a challenge at the forefront of the field of magnetic molecular materials [1–6]. Maintained interest in these compounds stems from their potential applications in data storage, molecular switching and sensing devices [7,8]. The ability to understand and control the SCO properties of molecular materials has been of ongoing interest and research. The intricate effect of intermolecular interactions and magnetic coupling on

the cooperativity of SCO systems has greatly complicated this understanding. Spin transition is generally observed in first-row transition metal coordination complexes with electronic configurations in the range d^4 – d^7 [9,10]. These transitions produce a change in the magnetic, optical and structural properties of the material. Most commonly, Fe(II) (d^6) is implemented in an approximately octahedral coordination environment, which, when in an appropriate ligand field, can undergo a transition from the paramagnetic ($S = 2$) high-spin (HS) state (5T_2) to a diamagnetic ($S = 0$) low-spin (LS) electronic configuration (1A_1) [11–14].

Advances in the design of large metallo-supramolecular complexes, utilising metal–ligand interactions to synthesise nanoscale architectures such as universal ravel, [15] molecular knots, [16,17] cages [18] and helices [19–21]—not so easily accessible through the use of covalent bonds—are providing SCO complexes with increasing complexity of design [22–24]. The development of synthetic pathways for the construction of metallo-supramolecular SCO architectures that do not require extensive ligand synthesis, and that utilise commercially available materials, provides greater accessibility of these materials for future applications of SCO materials [25].

Homoleptic tris-diimine moieties have been extensively explored as ligand donors in SCO complexes [26], with the 2,4-imidazole-imine functional groups commonly displaying SCO behaviour in Fe(II) complexes of this manner [24,27]. Imidazole-imine groups create N–H hydrogen-bond donor sites towards the exterior of the chemical structure, providing an increased potential for the organisation of the individual subunits into a larger network within the crystal structure, leading to magnetic cooperativity between molecular subunits [25].

To the best of our knowledge, there are only a few examples of Fe(II) dinuclear triple helicates that are capable of undergoing a reversible spin transition [25,28–32], all of which utilise the imidazole-imine moiety. Such compounds are composed of three ligands bridging two metal ion centres in a helical architecture. Hannon and co-workers explored the structural and magnetic differences of various counter ions and metal ion identities in a helicate series using carbon as the central atom of the ligand ($-\text{CH}_2-$) [25]. Two years later, the Mössbauer and magnetic properties of such complexes with the ClO_4^- counter ion were examined by Garcia and Gülich [28]. More recently, further studies of such helicates were conducted by Kruger [29,30], employing an oxygen central atom ($-\text{O}-$), identifying the importance of the degree of solvation on the spin transition of these compounds, as well as investigating the light-induced trapping of the excited state. Alternatively, the design and synthesis of coordination cages reported by Fujita [33], showed that the steric nature of the central atom of the ligand (C, S or O) could be manipulated to give subtly different ligand angles, which produced profound changes in the overall supramolecular architecture.

After investigations of such dinuclear Fe(II) SCO triple helicates, such as counter ions and solvents, this paper sought to synthesise three Fe(II) dinuclear triple helicates, $[\text{Fe}_2(\text{L}^1)_3](\text{BF}_4)_2$ (**1**), $[\text{Fe}_2(\text{L}^2)_3](\text{BF}_4)_2$ (**2**) and $[\text{Fe}_2(\text{L}^3)_3](\text{BF}_4)_2$ (**3**), and investigate the effects of the steric nature of three different central ligand atom identities ($-\text{X}-$, where $\text{X} = \text{CH}_2, \text{S}$ or O , Figure 1) on the structure and spin transition of their respective helicate architectures. Changing the identity of this central atom of the ligand may have several effects on the compounds. First, manipulation of the angle with which the ligand coordinates to two Fe(II) centres could influence the intra-helical separation ($\text{Fe}\cdots\text{Fe}$ separation). The investigation of the $-\text{CH}_2-$ compound, **1**, by Hannon and Gülich [25,28], found this separation to be 11.56 Å, while in the $-\text{O}-$ compounds of Kruger and co-workers the distances of 11.35 and 11.45 Å for compounds with MeCN and H_2O solvent inclusions were respectively exhibited. Second, slight changes in this angle could affect the geometry of the coordination environment (octahedral distortion), and therefore affect the temperature of transition [34]. Such structural manipulation could also cause a change in the preferred three-dimensional packing arrangement of the helicates in the crystal lattice, imposing changes on the intermolecular interactions within the crystal lattice and inter-helical Fe–Fe separation. These factors could all affect the cooperativity between the Fe(II) centres in the lattice, and as a result impact the spin-transition profile.

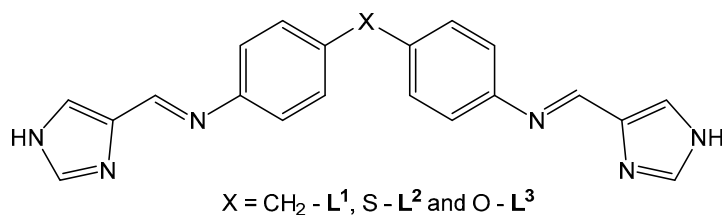


Figure 1. Schematic representation of the ligands L¹, L² and L³.

2. Results and Discussion

2.1. Syntheses

Three Schiff base bis-bidentate ligands L¹, L² and L³ were prepared in 88%, 91% and 93% yield, respectively, from the condensation of imidazole-4-carbaldehyde with 4,4-diaminodiphenylmethane, 4,4'-diaminobiphenyl sulfide or 4,4'-diaminodiphenyl ether. ¹H NMR spectra (Figures S1–S3) and high-resolution electrospray ionization (HR-ESI) mass spectrometry results were consistent with the proposed structures of L¹, L² and L³, with the NMR spectra, confirming the formation of bis-bidentate linking species. In the HR-mass spectra (Figures S4–S6), peaks for [Ligand+H]⁺ were observed at *m/z* 355.1606 (for [L¹+H]⁺), *m/z* 357.1367 (for [L²+H]⁺) and *m/z* 357.1325 (for [L³+H]⁺); the appropriate isotope patterns for [Ligand+H]⁺ were evident (inserts in Figures S4–S6) with the isotopic distributions in excellent agreement with their simulated patterns. The further reaction of L¹, L² and L³ with iron(II) tetrafluoroborate in acetonitrile, respectively, followed by the slow diffusion of diethyl ether into the reaction mixture, produced large light orange crystals of complexes **1**, **2** and **3** of suitable quality for X-ray diffraction studies. HR-ESI mass spectrometry results (Figures S7–S9) revealed a series of peaks of various charges corresponding to {[Fe₂(L^{*m*})₃][BF₄]_(4–*n*)}^{*n+*} (*m* = 1–3 and *n* = 2–4), which are consistent with the successive loss of [BF₄][−] anions, with the isotopic distributions for all the above species being in good agreement with their simulated patterns (inserts in Figures S7–S9). However, a singly charged species of {[Fe₂(L^{*m*})₃][BF₄]₃}⁺ (*m* = 1–3), resulting from the loss of one [BF₄][−] anion was not observed, even at low intensity for all three compounds.

2.2. Magnetic Susceptibility Measurements

Magnetic susceptibility data was collected over the temperature range of 50–350 K. The measurements were performed on polycrystalline samples with a field of 0.5 T; a scan rate of 4 K/min. The χ_{MT} versus *T* plots for the compounds **1**, **2** and **3** are shown in Figure 2. The samples were pre-dried for two weeks in a vacuum oven and heated to 400 K for 30 min in an initial heating cycle to remove acetonitrile solvent molecules included in the lattice (see DSC-TGA measurements Figures S10–S12). The samples were then cooled to 50 K and subsequently heated to 350 K. The heating and cooling modes demonstrated a small hysteresis for all three compounds **1–3** (Figures 2 and S19–S21).

The χ_{MT} versus *T* plot of **1**, in the cooling mode, is characteristic of a half SCO, with broad transition taking place between 60 and 250 K. The room temperature χ_{MT} of 7.71 cm³·K·mol^{−1} corresponds to two magnetically uncoupled octahedral Fe(II) centres with an ⁵T₂ (*S* = 2) ground state. As the temperature was lowered, the χ_{MT} stayed relatively constant until 240 K, after which it dropped in a single step manner, with a *T*_{1/2↓} value of 155 K, towards a value of 4.41 cm³·K·mol^{−1} at 50 K. This represents a slightly incomplete half spin transition, with approximately 40% of the Fe(II) centres transitioning to a LS¹A₁ (*S* = 0) state. Alternatively, the heating mode demonstrated a *T*_{1/2↑} value of 170 K, indicating a thermal hysteresis of 15 K.

The spin transition of **2** demonstrated a more abrupt character. For the cooling mode, the room temperature χ_{MT} value of 7.65 cm³·K·mol^{−1} was consistent with a full [HS–HS] state. Upon cooling, the χ_{MT} also decreased in a single step manner, with a *T*_{1/2↓} value of 115 K. At 50 K, the χ_{MT} value dropping to 3.15 cm³·K·mol^{−1}, which corresponded to c.a. 60% of the Fe(II) metal ions having

undergone a thermally-induced spin conversion to the low-spin 1A_1 ($S = 0$) from the high-spin 5T_2 ($S = 2$) electronic state. A similar thermal hysteresis of 15 K between the cooling and heating mode was observed ($T_{1/2} \uparrow 130$ K for heating mode).

Finally, **3** behaved in a similar manner, exhibiting a more gradual spin transition, with a $T_{1/2}$ of 150 K and 165 K for the cooling and heating cycles respectively, with a 15 K thermal hysteresis. The room temperature $\chi_M T$ value of $7.67 \text{ cm}^3 \cdot \text{K} \cdot \text{mol}^{-1}$ again showed complete [HS–HS] occupation of the Fe(II) centres. This decreased in a single step manner to a value of $3.92 \text{ cm}^3 \cdot \text{K} \cdot \text{mol}^{-1}$ at 50 K, at which point approximately 50% of Fe(II) had transitioned to the low spin state.

Of the three compounds, the sulphur derivative demonstrated the most complete half spin transition and a more abrupt nature. The carbon and oxygen derivatives exhibited very similar $\chi_M T$ versus T plots, although the oxygen derivative possessed a slightly more complete half transition.

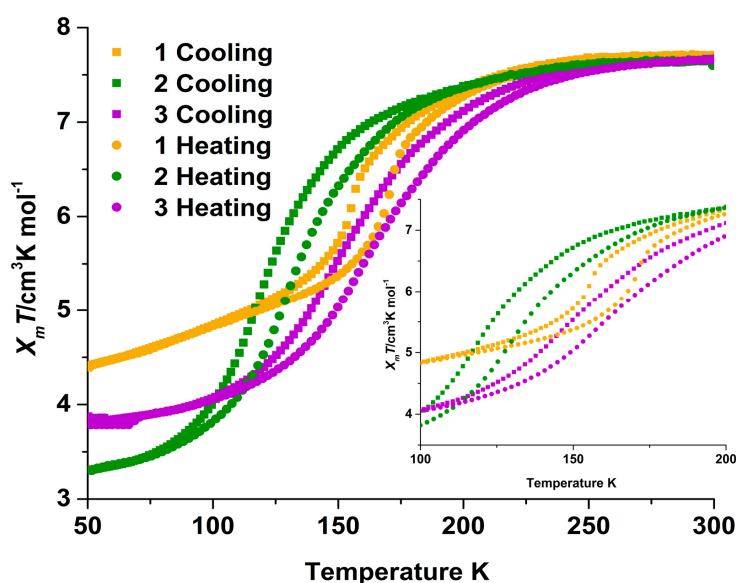


Figure 2. Magnetic susceptibility $\chi_M T$ versus T plots for **1–3**, at a scan rate of 4 K/min over the temperature range of 50–300 K, in both the cooling (square) and heating (circle) modes. For clarity, the inset shows the spin transition between 100 and 200 K.

2.3. Magneto-Structural Correlations

Single crystal X-ray diffraction experiments were performed at 100 K for **1**, **2** and **3** respectively (Figure 3). The complex **1**, which was previously reported by Hannon et al. [25] at 100 K, crystallised in the monoclinic space group $C2/c$, with half of the helicate in the asymmetric unit. The Fe(II) atom is coordinated by three N_{imine} and three $N_{\text{imidazole}}$ donors in a distorted octahedral environment, with octahedral distortion parameters (Σ) of 76.30 (Fe01) degrees (Table 1). The N–Fe(II) coordinate bond lengths were 2.12 Å (Fe01). These intermediate values suggest a mixed population of HS and LS-state Fe(II) centres within the helicates of the crystal lattice ([LS–HS]) at 100 K [29,30,34,35]. The two Fe(II) centres are separated by an inter-helical distance of 11.72 Å (Table 2). Hydrogen bonding interactions are present between the BF_4^- counter ions and the imidazole N–H ($\text{F} \cdots \text{N}$ 2.71 and 2.80 Å), as well as between acetonitrile C–H and counter ion F ($\text{C} \cdots \text{F}$ 2.71 Å).

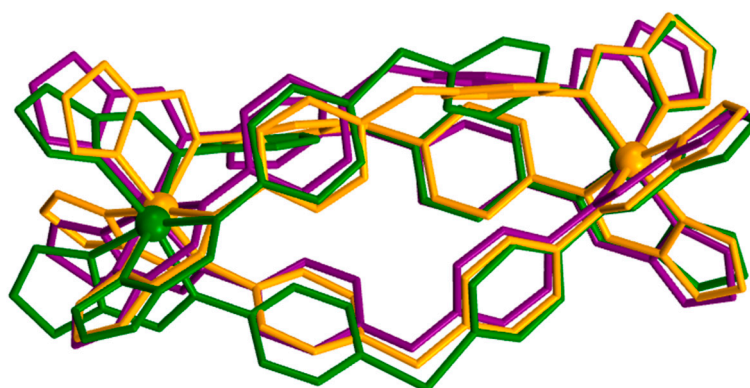


Figure 3. Schematic overlay representation of the X-ray structures of **1** (orange), **2** (green) and **3** (purple) at 100 K. Counter Ions, solvent molecules and hydrogen atoms have been excluded for clarity.

The complex **1** packs in infinite 2D sheets along the *c* and *a*-crystallographic axes in rows of helicates orientated in a diagonal manner with respect to the adjacent helicates along these axes (Figure 4). These 2D sheets stack upon one another along the *b*-axis in an offset manner. The observed differences in magnetic susceptibility results between **1** and those reported by Hannon et al. may be a result of the different packing arrangements these helicates demonstrate and the absence of the formation of a two-dimensional hydrogen-bonding network in **1**. As such, differences in molecular arrangement and non-covalent interactions leads to separate degrees of cooperativity between Fe(II) centres throughout the crystal lattice. The lesser extent to which counter ions provide intermolecular interactions between individual helicates may explain why the spin-crossover observed in this study is less abrupt in nature [36]. The asymmetric unit obtained by Hannon et al. contained two waters, two acetonitriles and one diisopropyl ether molecule, whereas the crystal structure of **1** contained only two partially occupied acetonitrile molecules in the asymmetric unit. The packing differences, along with the alternate solvent molecules, could have led to different degrees of cooperativity between Fe(II) centres of the crystal lattice. It is also to be noted that **1** was crystallised by means of a diethylether vapour diffusion, while Hannon et al. employed a diisopropyl ether diffusion.

The magnetic susceptibility measurement at 100 K ($4.84 \text{ K} \cdot \text{mol}^{-1}$) suggests approximately 40% of Fe(II) centres have transitioned to a low spin state. This is confirmed by crystal data measurements, which show Fe–N bond lengths and distortion parameters representative of a mixed spin-state population, [LS–HS], of Fe(II) centres. At this stage, single crystal diffraction experiments were unable to be performed at high temperatures.

Table 1. Comparison of important spin cross-over related crystallographic values.

Compound	Σ (Degrees)	Average Fe(II)–N Bond Lengths (Å)	High Spin or Low Spin Fe(II) in the Asymmetric Unit
1 100 K	Fe01—76.30	Fe01—2.13	1 mixed HS/LS-state population
2 100 K	Fe01—59.4 Fe02—90.3	Fe01—2.00 Fe02—2.18	1 HS, 1 LS
3 100 K	Fe01—77.2 Fe02—85.2	Fe01—2.10 Fe02—2.18	1 HS, 1 mixed HS/LS state population

Table 2. Comparison of helical geometric parameters in **1**, **2** and **3**.

Complex	-X- Angle (Degrees)	Intra-Helical Separation (Å)	Closest Inter-Helical Separation (Å)
1	113.6	11.72	8.71
2	104.9	11.78	8.31
3	115.8	11.62	7.96

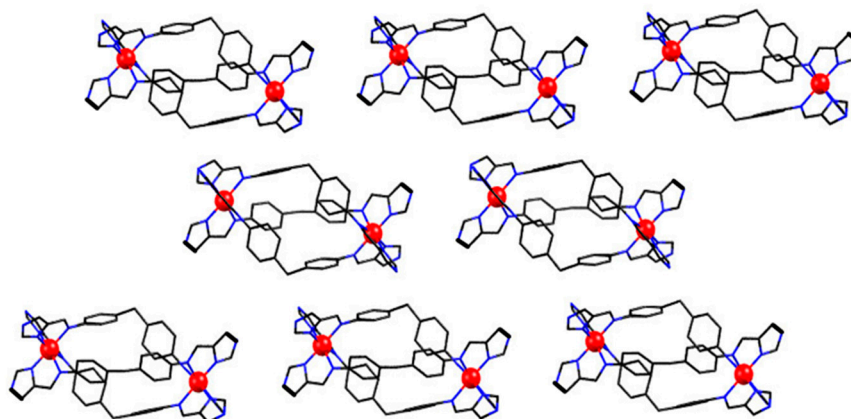


Figure 4. Schematic representation of the crystal packing structure of **1** at 100 K, demonstrating the formation of 2D sheets of interdigitated helicates. Solvent molecules and counter ions have been excluded for clarity. Mixed spin state populated Fe(II) metal centres are represented by red spheres. The crystallographic *c*-axis runs along the length of the page, and the *a*-axis down the page.

At 100 K, complex **2** crystallised in the triclinic space group $P\bar{1}$. A single unique helicate was present in the asymmetric unit, encompassing one high-spin and one low-spin Fe(II) centre (Figure 5). This is confirmed by average Σ values of 90.3 and 59.4 degrees and the average Fe(II)–N distances of 2.18 and 2.00 Å for the HS and LS Fe(II) centres respectively [34,35,37], which is consistent with magnetic measurements that suggest a 53% transition to the low spin state at 100 K ($\chi_M T$ 7.67 cm³·K·mol⁻¹). The intra-helical distance in this case is 11.78 Å. These helicates are linked by hydrogen bonding between the uncoordinated N_{Imidazole} N–H and BF₄⁻ counter ions (F···N 2.78 and 2.90 Å) along the *a*-axis. Along this axis, the adjacent centres linked by hydrogen-bonding are of the same spin-state. Packing along the *c*-axis lengthwise, in a slightly interdigitated manner, positions the closest Fe(II) centres of adjacent helicates so that they are of the opposite spin state (inter-helical distance 12.31 Å) (Figure 5). Similarly, along the *b*-axis, inversion of the complexes produces alternating HS and LS Fe(II) centres, so that centres of opposite spin states are closest to one another (inter-helical distance 8.31 Å) (Figure 6). This is considerably closer than the intra-helical distance between Fe(II) metal ions (Table 2). In this manner, the high and low spin states alternate throughout the crystal lattice at 100 K. The helicates are not linked by hydrogen bonding along the *b* or *c*-axis. Hydrogen-bonding interactions linking complexes of like spin-states along the *a*-axis suggest some degree of cooperativity between Fe(II) centres along this crystallographic axis. Three of the six aryl substituents participate in intramolecular edge-to-face CH··· π interactions, stabilising larger torsion angles between planes of the two phenyl groups of the same ligand.

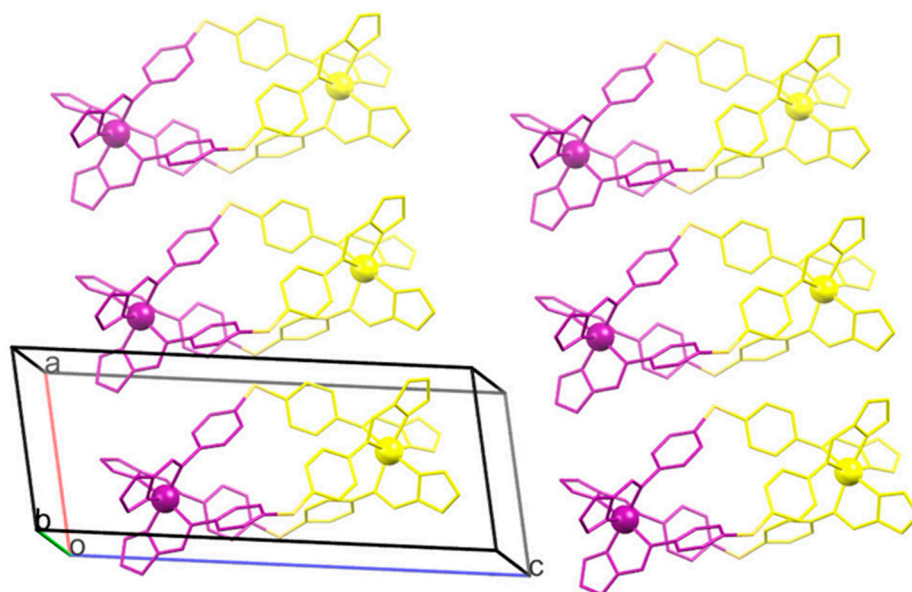


Figure 5. Schematic representation of the X-ray crystal structure of **2** at 100 K showing the distribution of high (yellow) and low spin (purple) Fe(II) centres along the crystallographic *c*- and *a*-axis. Hydrogens, solvent and counter ions have been excluded for clarity.

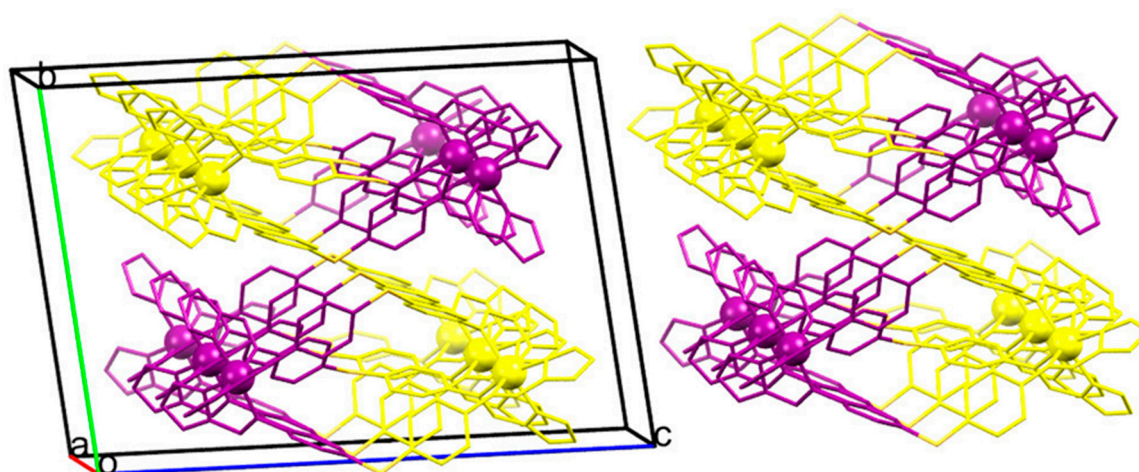


Figure 6. Schematic representation of the X-ray crystal structure of **2** at 100 K showing the distribution of high (yellow) and low spin (purple) Fe(II) centres in alternating HS and LS centres along the *b*- and *c*-axis, and in chains of the same spin state along the *a*-axis. Hydrogens, solvent and counter ions have been excluded for clarity.

Finally, complex **3** at 100 K also crystallised in the triclinic space group $P\bar{1}$, with one molecule in the asymmetric unit. The Σ octahedral distortion and Fe–N bond lengths in this case suggest one HS and one mixed spin state populated Fe(II) centre (2.18 and 2.10 Å and Σ values of 85.2 and 77.2 degrees). Again, this agrees with the magnetic susceptibility data at 100 K ($4.07 \text{ cm}^3 \cdot \text{K} \cdot \text{mol}^{-1}$), which indicates that around 53% of Fe(II) centres are in the HS state. At 100 K, the complex packs in undulating layers of complexes along the crystallographic *a*-axis. Along the *a* and *b*-axis, the Fe(II) centres in neighbouring helicates pack so that they are adjacent to Fe(II) ions of the same spin state (Figure 7). These form infinite row-like domains of Fe(II) atoms throughout the lattice with the same spin state. Hydrogen bonding interactions between non-bonding imidazole nitrogens and BF_4^- counter ions ($\text{F} \cdots \text{N}$ 2.87, 2.74, 2.89 and 2.83 Å) link HS centres to mixed-spin state centres of adjacent complexes

along the *c*-axis. The intra-helical Fe⋯Fe separation is 11.62 Å, while the shortest inter-helical distance is 7.96 Å. This intra-helical distance is very similar to that found by Archer et al. [30] in an oxygen helicate derivative with methylated imidazole moieties. Two of the six aryl rings of the dincular triple helicate participate in edge-to-face CH⋯π interactions of 2.54 and 2.83 Å.

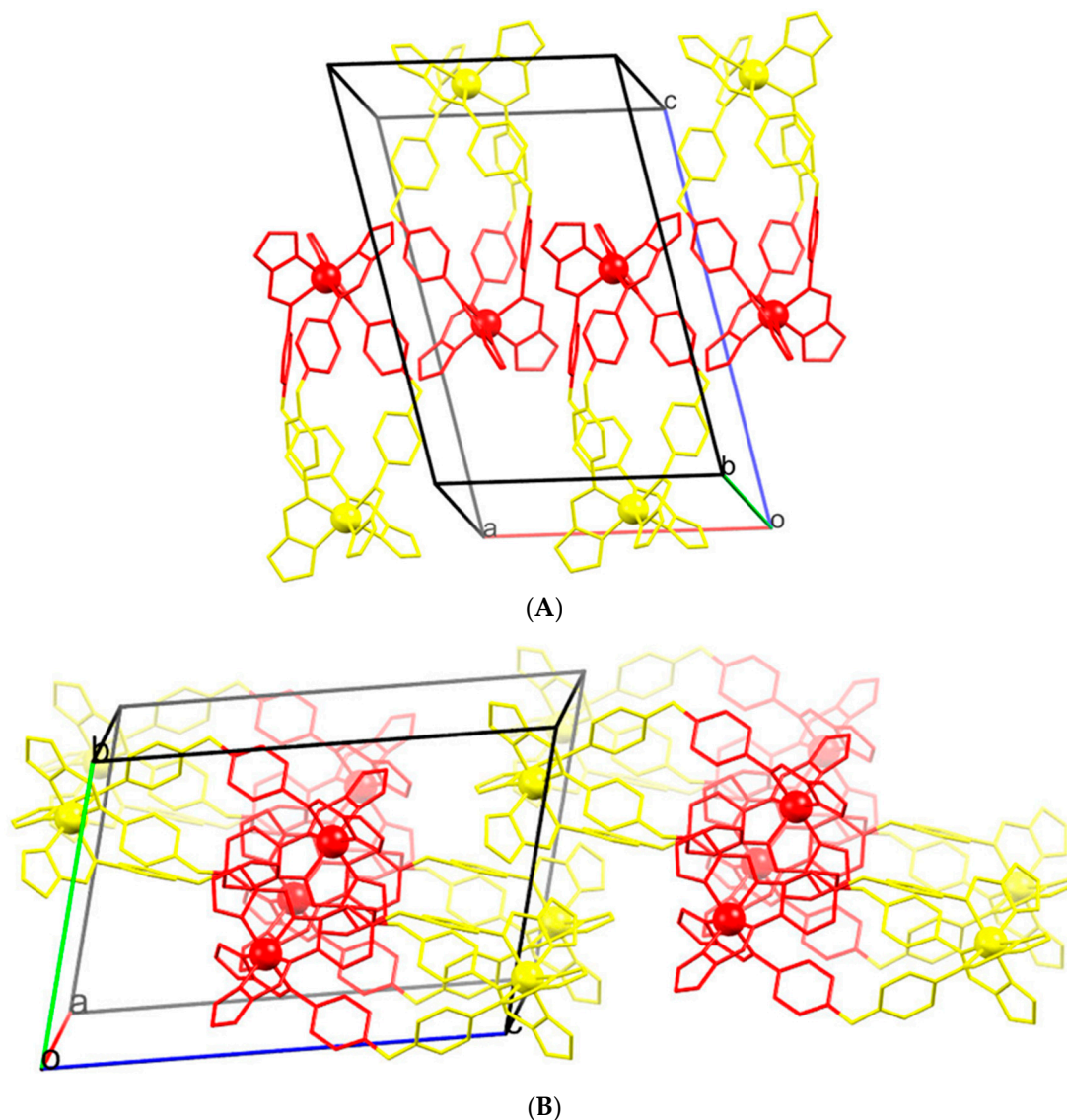


Figure 7. Schematic representations of the crystal packing structure of **3** at 100 K showing the packing of HS (yellow) and mixed spin state (red) Fe(II) centres in undulating rows of metal ions with similar spin states throughout the crystal lattice. Image (A) shows the packing in two-dimensions and image (B) shows three-dimensional arrangement of Fe(II) centres. Hydrogens, solvent and counter ions have been omitted for clarity.

This study was interested in how the angle formed between the linking atom (C, S or O) and the two phenyl rings of the ligand (–X–, where X = CH₂, S or O) affects the nature of the spin transition. Differences in this angle could influence the spin transition by altering the intra-helical distance, or by altering the orientation with which the complexes pack, therefore changing the degree of intermolecular interactions and cooperativity between metal centres. The –X– ligand angle was largest for the –O– in **3** (115.760 degrees), while –CH₂– (**1**) and –S– (**2**) were 113.6 and 104.9 degrees respectively. The packing orientations of the three structures at 100 K differ significantly. This could be a factor of the intra-helical

distance and other geometric properties of the helicates, as well as the different intermolecular interactions with solvent and counter ion molecules. Interestingly, the magnetic susceptibility curves of **1** and **3** are very similar in shape ($T_{1/2} \downarrow$ 155 and 150 K respectively), as are their $-X-$ angles. On the other hand, **2** displayed a much steeper curve ($T_{1/2} \downarrow$ 115 K), and in turn a larger intra-helical separation. Complex **2** also displayed a greater degree of intermolecular interactions mediated by the BF_4^- anions, linking the helicates into chains along the a -axis. In this structure, these “linked” Fe(II) centres were of the same spin-state (see above), suggesting a greater degree of cooperativity between Fe(II) centres in this structure. As has been shown previously, the intermolecular interactions, particularly hydrogen bonding, are a crucial influence on the cooperativity of the spin transition [36,38,39]. This cooperativity may be a factor influencing the more abrupt nature of the spin transition in **2**. To surmise, altering the steric nature of the central ligand atom (C, O or S) shows a slight influence on the spin transition, allowing the spin transition to be altered in this manner. Although the direct cause of this difference is not clear, it is more likely to be a consequence of subtle changes in the packing arrangement, the inter and intra-helical separations, as well as the degree of intermolecular interactions within the crystal structure. Important crystallographic information for compounds **1**, **2** and **3** is included in Table 3.

Table 3. Crystallographic data for the compounds measured in this experiment.

	1·(CH ₃ CN)	2·2 (CH ₃ CN)	3·2 (CH ₃ CN)
Empirical formula	C ₆₅ H ₅₇ B ₄ F ₁₆ Fe ₂ N ₁₉	C ₆₄ H ₅₄ B ₄ F ₁₆ Fe ₂ N ₂₀ S ₃	C ₆₄ H ₅₄ B ₄ F ₁₆ Fe ₂ N ₂₀ O ₃
Formula weight	1563.23	1658.39	1610.21
Temperature/K	100	100	100
Crystal system	monoclinic	triclinic	triclinic
Space group	C2/c	P $\bar{1}$	P $\bar{1}$
$a/\text{\AA}$	21.131(4)	9.5210(19)	13.837(3)
$b/\text{\AA}$	17.391(4)	16.723(3)	13.855(3)
$c/\text{\AA}$	21.069(4)	23.621(5)	20.684(4)
$\alpha/^\circ$	90	95.29(3)	77.43(3)
$\beta/^\circ$	107.00(3)	100.29(3)	77.58(3)
$\gamma/^\circ$	90	92.93(3)	86.73(3)
Volume/ \AA^3	7404(3)	3675.8(13)	3779.5(15)
Z	4	2	2
$\rho_{\text{calc.}}/\text{g/cm}^3$	1.402	1.498	1.415
μ/mm^{-1}	0.485	0.576	0.481
$F(000)$	3184.0	1684.0	1636.0
2 θ range for data collection/ $^\circ$	0.02 \times 0.01 \times 0.01	0.015 \times 0.0075 \times 0.0075	0.02 \times 0.01 \times 0.01
Index ranges	Synchrotron ($\lambda = 0.7108$)	Synchrotron ($\lambda = 0.7108$)	Synchrotron ($\lambda = 0.7108$)
Reflections collected	3.09 to 52.998	1.762 to 52.742	2.062 to 53.998
Independent reflections	$-26 \leq h \leq 26, -21 \leq k \leq 21,$ $-26 \leq l \leq 26$	$-11 \leq h \leq 11, -20 \leq k \leq 20,$ $-29 \leq l \leq 29$	$-17 \leq h \leq 17, -17 \leq k \leq 17,$ $-26 \leq l \leq 26$
Data/restraints/parameters	50,460	45,853	57,096
Goodness-of-fit on F^2	6995 [$R_{\text{int}} = 0.0697,$ $R_{\text{sigma}} = 0.0341$]	13,521 [$R_{\text{int}} = 0.0971,$ $R_{\text{sigma}} = 0.0898$]	14,860 [$R_{\text{int}} = 0.0446,$ $R_{\text{sigma}} = 0.0360$]
Final R indexes [$I \geq 2\sigma(I)$]	6995/218/630	13,521/202/1047	14,860/33/1095
Final R indexes [all data]	1.119	1.157	1.072
Largest diff. peak/hole/ $e \text{\AA}^{-3}$	$R_1 = 0.1050, wR_2 = 0.2997$	$R_1 = 0.1103, wR_2 = 0.2958$	$R_1 = 0.0691, wR_2 = 0.1967$

3. Materials and Methods

All reagents and solvents were purchased from commercial sources, with no further purification being undertaken. ¹H NMR spectra were recorded on a Bruker 400 MHz spectrometer (Bruker AXS GmbH, Karlsruhe, Germany). High resolution ESI-MS data were acquired using a Waters Xevo QToF mass spectrometer (Waters, Milford, MA, USA), operating in positive ion mode with a desolvation temperature of 120, desolvation gas flow of 450 and varying sample and extraction cone temperatures. A waters lock spray system was used to calibrate the high-resolution masses. FT-IR measurements were undertaken on a Bruker Vertex 70 (Bruker AXS GmbH, Karlsruhe, Germany) with a diamond ATR stage. DSC and TGA measurements were performed using a simultaneous thermal analysis (STA) 449 C Jupiter instrument (Netzsch Australia Pty Ltd., Sydney, Australia). The STA measurements were

performed using an aluminium crucible; nitrogen was used as both the protective and purge gases, and the temperature range of 30–200 °C was cycled at a rate of 10·K·min⁻¹.

3.1. Preparation of (L¹, L² and L³)

The methanol (15 mL) solution of 0.75 mmol of 4,4'-methylenedianiline, 4,4'-oxydianiline or 4,4'-thiodianiline was added dropwise to 1.50 mmol of imidazole-4-carbaldehyde in 15 mL methanol under stirring. Three drops of glacial acetic acid were added and the reaction mixture was refluxed overnight. The mixture was allowed to cool to room temperature, and subsequently cooled in a refrigerator. The white precipitate was filtered, washed with MeOH and air dried.

L¹: Yield 88%. ¹H NMR (DMSO, 400 MHz) δ (ppm) 8.44 (s, 2H), 7.83 (s, 2H), 7.65 (br, 2H), 7.26 (d, 4H), 7.14 (d, 4H), 3.95 (s, 2H); ESI-MS (positive-ion detection, CH₃CN, *m/z*): calcd. for [L¹+H]⁺, 355.1671; found 355.1606; FT-IR (ATR ν_{max}/cm⁻¹): 3023, 2821, 1626, 1501, 1221, 1093, 873, 841, 620, 537 cm⁻¹.

L²: Yield 91%. ¹H NMR (DMSO, 400 MHz) δ (ppm) 8.46 (s, 2H), 7.83 (d, 3H), 7.56 (br, 1H), 7.36 (d, 4H), 7.23 (d, 4H); ESI-MS (positive-ion detection, CH₃CN, *m/z*): calcd. for [L²+H]⁺, 373.1235; found 373.1167; FT-IR (ATR ν_{max}/cm⁻¹): 2579, 1622, 1491, 1243, 1111, 834, 622, 535 cm⁻¹.

L³: Yield 93%. ¹H NMR (DMSO, 400 MHz) δ (ppm) 8.45 (s, 2H), 7.84 (s, 2H), 7.26 (d, 4H), 7.04 (d, 4H), 3.38 (s), 2.51 (p); ESI-MS (positive-ion detection, CH₃CN, *m/z*): calcd. for [L³+H]⁺, 357.1464; found 357.1325; FT-IR (ATR ν_{max}/cm⁻¹): 2583, 1630, 1578, 1364, 1110, 1087, 867, 821, 777, 620, 552 cm⁻¹.

3.2. Preparation of 1, 2 and 3

Fe(BF₄)₂·6H₂O (0.2 mmol) in 10 mL of acetonitrile was slowly added to a suspension of L¹, L² or L³ (0.3 mmol) in 20 mL of acetonitrile. The reaction mixture was heated at 70 °C and stirred for 3 h, leading to a clear orange solution. The solution was filtered, with a slow diffusion of diethyl ether into the acetonitrile solution, resulting in the formation of large orange crystals. These were then allowed to dry under vacuum. Single crystals were taken from the same sample and used for the X-ray study.

1: Yield 81%. ESI-HRMS (positive ion detection, CH₃CN, *m/z*): calcd. for [Fe₂(L¹)₂]⁴⁺, 293.5881; found 293.5724; FT-IR (ATR ν_{max}/cm⁻¹): 3311, 1619, 1491, 1225, 1006, 613 cm⁻¹.

2: Yield 78%. ESI-HRMS (positive-ion detection, CH₃CN, *m/z*): calcd. for [Fe₂(L²)₂]⁴⁺, 307.0554; found 307.0481; FT-IR (ATR ν_{max}/cm⁻¹): 3310, 2981, 1615, 1004, 613, 562 cm⁻¹.

3: Yield 85%. ESI-HRMS (positive-ion detection, CH₃CN, *m/z*): calcd. for [Fe₂(L³)₂]⁴⁺, 295.0726; found 295.0609; FT-IR (ATR ν_{max}/cm⁻¹): 3310, 3150, 1618, 1490, 1225, 1200, 1007, 861, 838, 613, 520 cm⁻¹.

3.3. X-ray Crystallography

The X-ray crystallography experiments were performed at the Australian Synchrotron, using silicon double crystal monochromated radiation at 100 K [40,41]. The crystal was rotated through Phi angle of 1–360 degrees. Data was collected at 100 K for each structure. Data integration and reduction was undertaken with XDS [42]. An empirical absorption correction was then applied using SADABS at the Australian Synchrotron [43]. The structures were solved by direct methods and the full-matrix least-squares refinements were carried out using a suite of SHELX programs [44,45] via the OLEX2 graphical interface [46]. Non-hydrogen atoms were refined anisotropically. Carbon-bound hydrogen atoms were included in idealised positions and refined using a riding model. The crystallographic data in CIF format has been deposited at the Cambridge Crystallographic Data Centre with CCDC 1568781–1568783. It is available free of charge from the Cambridge Crystallographic Data Centre, 12 Union Road, Cambridge CB2 1 EZ, UK; fax: (+44) 1223-336-033; or e-mail: deposit@ccdc.cam.ac.uk. Specific refinement details and crystallographic data for each structure are present above and in the supporting information. The asymmetric unit of **1** contains one half of a helicate, two BF₄⁻ counter ions and two acetonitrile molecules, with occupancies of 0.25. One counter ion was modelled in two parts, one of 0.8 and one of 0.2 occupancies, the latter of which was modelled isotropically. Both solvent molecules were modelled isotropically. Compound **2** possessed one helicate, four BF₄⁻ counter ions and two acetonitrile solvent molecules. Disorder in two BF₄⁻ counter ions were modelled in two parts.

Compound **3** possessed an asymmetric unit with one full helicate, four BF_4^- counter ions and four acetonitrile molecules with an occupancy of 0.5 each, one of which was modelled in two parts of 0.25 occupancy. These later two were modelled isotropically.

3.4. Magnetic Susceptibility Measurements

Samples of crystalline material were dried for two weeks in a vacuum oven at 340 K prior to magnetic measurement. Data for magnetic susceptibility measurements were collected on a Quantum Design Versalab Measurement System (Quantum Design, San Diego, CA, USA) with a Vibrating Sample Magnetometer (VSM) attachment. Measurements were taken continuously under an applied field of 0.5 T. For each experiment, samples were first heated in situ to 400 K for 30 min to ensure complete solvent loss, and subsequently cycled over the temperature range 50–350 K at a heating rate of $4 \text{ K}\cdot\text{min}^{-1}$.

4. Conclusions

In conclusion, a series of two novel and one previously studied Fe(II) dinuclear triple helicates was presented, utilising a homoleptic tris-2,4-diimine coordination environment to induce a low temperature spin transition. The identity of the central atom of the ligand was changed to deduce the effects of the different steric nature of these ligands on the structure and spin-transition profile of these compounds (**1**, **2** and **3**). All three compounds displayed a transition of approximately half of the Fe(II) centres at 50 K. Compound **1** (– CH_2 –), **2** (–S–) and **3** (–O–) completed a transition of 40%, 60% and 50% of Fe(II) ions to the $S = 0$ LS state respectively at 50 K, with a $T_{1/2\downarrow}$ value of 150, 115 and 155 K in the cooling mode, and thermal hysteresis of 15 K for **1**, **2** and **3**. Compound **2** showed the most complete and abrupt spin transition. The three compounds crystallised in the same space group, although displayed different packing arrangements, intermolecular interactions and arrangements of HS and LS centres throughout the lattice. The ligand (–X–) angle was found to be 113.6, 104.9 and 115.8 degrees for compounds **1**, **2** and **3** respectively, corresponding to intra-helical Fe...Fe separations of 11.72, 11.79 and 11.62 Å. Changing the steric nature of the central ligand atom (C, S or O) produced helicate complexes with slight differences in their magnetic behaviours, which allows the magnetic properties of these materials to be altered in this way. Although the direct mechanism of this change cannot be confirmed and is likely to be the result of changes in crystal packing, the degree of intermolecular interactions, intra-helical distances and the electronic effects of the substituted ligand central atoms could cause differing degrees of cooperativity between Fe(II) metal centres.

Supplementary Materials: The following are available online at www.mdpi.com/2304-6740/5/4/62/s1. Experimental data for HRESI-MS, FT-IR, NMR and TGA-DSC, cif and cif-checked files.

Acknowledgments: The authors would like to thank the Western Sydney University (WSU) for research funding, the Advanced Characterization Facility at WSU and Sydney University at which the magnetic measurements were performed. Alexander R. Craze would like to thank WSU and The Australian nuclear Science and Technology Organization (ANSTO) for Masters Scholarships. The crystallographic data were undertaken on the MX1 beamline of the Australian Synchrotron, Clayton, Victoria, Australia. We also thank Australian Synchrotron for travel support and their staff for beamline assistance.

Author Contributions: Alexander R. Craze performed the synthetic, experimental, single crystal X-ray and magnetic studies. Natasha F. Sciortino and Cameron J. Keperter assisted in the magnetic studies. Mohan M. Badbhade and Christopher E. Marjo assisted with crystallographic studies. Alexander R. Craze and Feng Li prepared the manuscript, and Feng Li directed the work.

Conflicts of Interest: The authors declare no conflict of interest.

References

1. Gütllich, P.; Gaspar, A.B.; Garcia, Y. Spin state switching in iron coordination compounds. *Beilstein J. Org. Chem.* **2013**, *9*, 342–391. [[CrossRef](#)] [[PubMed](#)]
2. Brooker, S. Spin crossover with thermal hysteresis: Practicalities and lessons learnt. *Chem. Soc. Rev.* **2015**, *44*, 2880–2892. [[CrossRef](#)] [[PubMed](#)]

3. Halcrow, M.A. Structure: Function relationships in molecular spin-crossover complexes. *Chem. Soc. Rev.* **2011**, *40*, 4119–4142. [[CrossRef](#)] [[PubMed](#)]
4. Bousseksou, A.; Molnár, G.; Salmon, L.; Nicolazzi, W. Molecular spin crossover phenomenon: Recent achievements and prospects. *Chem. Soc. Rev.* **2011**, *40*, 3313–3335. [[CrossRef](#)] [[PubMed](#)]
5. Leita, B.A.; Moubaraki, B.; Murray, K.S.; Smith, J.P.; Cashion, J.D. Structure and magnetism of a new pyrazolate bridged iron(II) spin crossover complex displaying a single HS–HS to LS–LS transition. *Chem. Commun.* **2004**, 156–157. [[CrossRef](#)] [[PubMed](#)]
6. Toftlund, H. Spin equilibrium in solutions. *Monatshfte Chem.* **2001**, *132*, 1269–1277. [[CrossRef](#)]
7. Kahn, O.; Martinez, C.J. Spin-Transition Polymers: From Molecular Materials toward Memory Devices. *Science* **1998**, *279*, 44–48. [[CrossRef](#)]
8. Halcrow, M.A. *Spin-Crossover Materials: Properties and Applications*; John Wiley & Sons Ltd.: Oxford, UK, 2013. [[CrossRef](#)]
9. Hayami, S.; Shigeyoshi, Y.; Akita, M.; Inoue, K.; Kato, K.; Osaka, K.; Takata, M.; Kawajiri, R.; Mitani, T.; Maeda, Y. Reverse Spin Transition Triggered by a Structural Phase Transition. *Angew. Chem. Int. Ed. Engl.* **2005**, *44*, 4899–4903. [[CrossRef](#)] [[PubMed](#)]
10. Hayami, S.; Moriyama, R.; Shigeyoshi, Y.; Kawajiri, R.; Mitani, T.; Akita, M.; Inoue, K.; Maeda, Y. Spin-Crossover Cobalt(II) Compound with Banana-Shaped Structure. *Inorg. Chem.* **2005**, *44*, 7295–7297. [[CrossRef](#)] [[PubMed](#)]
11. Zhao, X.-H.; Zhang, S.-L.; Shao, D.; Wang, X.-Y. Spin Crossover in $[\text{Fe}(\text{2-Picolylamine})_3]^{(2+)}$ Adjusted by Organosulfonate Anions. *Inorg. Chem.* **2015**, *54*, 7857–7867. [[CrossRef](#)] [[PubMed](#)]
12. Dupouy, G.; Marchivie, M.; Triki, S.; Sala-Pala, J.; Gómez-García, C.J.; Pillet, S.; Lecomte, C.; Letard, J.-F. Photoinduced HS state in the first spin-crossover chain containing a cyanocarbanion as bridging ligand. *Chem. Commun.* **2009**, 3404–3406. [[CrossRef](#)] [[PubMed](#)]
13. Garcia, Y.; Niel, V.; Muñoz, M.C.; Real, J.A. Spin Crossover in 1D, 2D and 3D Polymeric Fe(II) Networks. In *Spin Crossover in Transition Metal Compounds I*; Gütllich, P., Goodwin, H.A., Eds.; Springer: Heidelberg/Berlin, Germany, 2004; pp. 229–257.
14. Gütllich, P.; Garcia, Y.; Goodwin, H.A. Spin crossover phenomena in Fe(II) complexes. *Chem. Soc. Rev.* **2000**, *29*, 419–427. [[CrossRef](#)]
15. Li, F.; Clegg, J.K.; Lindoy, L.F.; Macquart, R.B.; Meehan, G.V. Metallosupramolecular self-assembly of a universal 3-ravel. *Nat. Commun.* **2011**, *2*, 1208. [[CrossRef](#)] [[PubMed](#)]
16. Baxter, P.N.W.; Lehn, J.-M.; Sleiman, H.; Rissanen, K. Multicomponent Self-Assembly: Generation and Crystal Structure of a Trimetallic[4]Pseudorotaxane. *Angew. Chem. Int. Ed.* **1997**, *36*, 1294–1296. [[CrossRef](#)]
17. Sleiman, H.; Baxter, P.N.W.; Lehn, J.-M.; Airola, K.; Rissanen, K. Multicomponent Self-Assembly: Generation of Rigid-Rack Multimetallic Pseudorotaxanes. *Inorg. Chem.* **1997**, *36*, 4734–4742. [[CrossRef](#)] [[PubMed](#)]
18. Ward, M.D.; Raithby, P.R. Functional behaviour from controlled self-assembly: Challenges and prospects. *Chem. Soc. Rev.* **2013**, *42*, 1619–1636. [[CrossRef](#)] [[PubMed](#)]
19. Hannon, M.J.; Childs, L.J. Helices and Helicates: Beautiful Supramolecular Motifs with Emerging Applications. *Supramol. Chem.* **2004**, *16*, 7–22. [[CrossRef](#)]
20. Albrecht, M. “Let’s Twist Again” Double-Stranded, Triple-Stranded, and Circular Helicates. *Chem. Rev.* **2001**, *101*, 3457–3498. [[CrossRef](#)] [[PubMed](#)]
21. Hora, S.; Hagiwara, H. High-Temperature Wide Thermal Hysteresis of an Iron(II) Dinuclear Double Helicate. *Inorganics* **2017**, *5*, 49. [[CrossRef](#)]
22. Breuning, E.; Ruben, M.; Lehn, J.-M.; Renz, F.; Garcia, Y.; Ksenofontov, V.; Gütllich, P.; Wegelius, E.; Rissanen, K. Spin Crossover in a Supramolecular Fe_4^{II} [2×2] Grid Triggered by Temperature, Pressure, and Light. *Angew. Chem. Int. Ed.* **2000**, *39*, 2504–2507. [[CrossRef](#)]
23. Struch, N.; Bannwarth, C.; Ronson, T.K.; Lorenz, Y.; Mienert, B.; Wagner, N.; Engeser, M.; Bill, E.; Puttredy, R.; Rissanen, K.; et al. An Octanuclear Metallosupramolecular Cage Designed To Exhibit Spin-Crossover Behavior. *Angew. Chem. Int. Ed.* **2017**, *56*, 4930–4935. [[CrossRef](#)] [[PubMed](#)]
24. Li, L.; Saigo, N.; Zhang, Y.; Fanna, D.J.; Shepherd, N.D.; Clegg, J.K.; Zheng, R.; Hayami, S.; Lindoy, L.F.; Aldrich-Wright, J.R.; et al. A large spin-crossover $[\text{Fe}_4\text{L}_4]^{8+}$ tetrahedral cage. *J. Mater. Chem. C* **2015**, *3*, 7878–7882. [[CrossRef](#)]
25. Tuna, F.; Lees, M.R.; Clarkson, G.J.; Hannon, M.J. Readily prepared metallo-supramolecular triple helicates designed to exhibit spin-crossover behaviour. *Chem. Eur. J.* **2004**, *10*, 5737–5750. [[CrossRef](#)] [[PubMed](#)]

26. Phan, H.; Hrudka, J.J.; Igimbayeva, D.; Lawson Daku, L.M.; Shatruk, M. A Simple Approach for Predicting the Spin State of Homoleptic Fe(II) Tris-diimine Complexes. *J. Am. Chem. Soc.* **2017**, *139*, 6437–6447. [[CrossRef](#)] [[PubMed](#)]
27. Fujinami, T.; Nishi, K.; Matsumoto, N.; Iijima, S.; Halcrow, M.A.; Sunatsuki, Y.; Kojima, M. 1D and 2D assembly structures by imidazole...chloride hydrogen bonds of iron(II) complexes $[\text{Fe}^{\text{II}}(\text{HL}^{n\text{-Pr}})_3]\text{Cl}\cdot\text{Y}$ ($\text{HL}^{n\text{-Pr}}$ = 2-methylimidazol-4-yl-methylideneamino-*n*-propyl; Y = AsF_6 , BF_4) and their spin states. *Dalton Trans.* **2011**, *40*, 12301–12309. [[CrossRef](#)] [[PubMed](#)]
28. Garcia, Y.; Grunert, C.M.; Reiman, S.; van Campenhoutd, O.; Gütllich, P. The Two-Step Spin Conversion in a Supramolecular Triple Helicate Dinuclear Iron(II) Complex Studied by Mössbauer Spectroscopy. *Eur. J. Inorg. Chem.* **2006**, *2006*, 3333–3339. [[CrossRef](#)]
29. Pelleteret, D.; Clérac, R.; Mathonière, C.; Harté, E.; Schmitt, W.; Kruger, P.E. Asymmetric spin crossover behaviour and evidence of light-induced excited spin state trapping in a dinuclear iron(II) helicate. *Chem. Commun.* **2009**, *2*, 221–223. [[CrossRef](#)] [[PubMed](#)]
30. Archer, R.J.; Hawes, C.S.; Jameson, G.N.L.; McKee, V.; Moubaraki, B.; Chilton, N.F.; Murray, K.S.; Kruger, P.E. Partial spin crossover behaviour in a dinuclear iron(II) triple helicate. *Dalton Trans.* **2011**, *40*, 12368–12373. [[CrossRef](#)] [[PubMed](#)]
31. Telfer, S.G.; Bocquet, B.; Williams, A.F. Thermal Spin Crossover in Binuclear Iron(II) Helicates: Negative Cooperativity and a Mixed Spin State in Solution. *Inorg. Chem.* **2001**, *40*, 4818–4820. [[CrossRef](#)] [[PubMed](#)]
32. Fujita, K.; Kawamoto, R.; Tsubouchi, R.; Sunatsuki, Y.; Kojima, M.; Iijima, S.; Matsumoto, N. Spin States of Mono- and Dinuclear Iron(II) Complexes with Bis(imidazolylimine) Ligands. *Chem. Lett.* **2007**, *36*, 1284–1285. [[CrossRef](#)]
33. Sun, Q.-F.; Iwasa, J.; Ogawa, D.; Ishido, Y.; Sato, S.; Ozeki, T.; Sei, T.; Yamaguchi, K.; Fujita, M. Self-Assembled $\text{M}_{24}\text{L}_{48}$ Polyhedra and Their Sharp Structural Switch upon Subtle Ligand Variation. *Science* **2010**, *328*, 1144–1147. [[CrossRef](#)] [[PubMed](#)]
34. Marchivie, M.; Guionneau, P.; Létard, J.-F.; Chasseau, D. Photo-induced spin-transition: The role of the iron(II) environment distortion. *Acta Crystallogr. Sect. B* **2005**, *61*, 25–28. [[CrossRef](#)] [[PubMed](#)]
35. Dupouy, G.; Marchivie, M.; Triki, S.; Sala-Pala, J.; Salaün, J.-Y.; Gómez-García, C.J.; Guionneau, P. The Key Role of the Intermolecular π - π Interactions in the Presence of Spin Crossover in Neutral $[\text{Fe}(\text{abpt})_2\text{A}_2]$ Complexes (A = Terminal Monoanion N Ligand). *Inorg. Chem.* **2008**, *47*, 8921–8931. [[CrossRef](#)] [[PubMed](#)]
36. Milin, E.; Benaïcha, B.; El Hajj, F.; Patinec, V.; Triki, S.; Marchivie, M.; Gomez-Garcia, C.J.; Pillet, S. Magnetic Bistability in Macrocyclic-Based Fe(II) Spin-Crossover Complexes: Counter Ion and Solvent Effects. *Eur. J. Inorg. Chem.* **2016**, *34*, 5305–5314. [[CrossRef](#)]
37. Guionneau, P.; Gac, F.L.; Lakhoufi, S.; Kaiba, A.; Chasseau, D.; Létard, J.-F.; Negrier, P.; Mondieig, D.; Howard, J.A.K.; Leger, J.-M. X-ray diffraction investigation of a spin crossover hysteresis loop. *J. Phys.* **2007**, *19*, 326211. [[CrossRef](#)]
38. Harding, D.J.; Phonsri, W.; Harding, P.; Gass, I.A.; Murray, K.S.; Moubaraki, B.; Cashion, J.D.; Liu, L.; Telfer, S.G. Abrupt spin crossover in an iron(III) quinolylsalicylaldimine complex: Structural insights and solvent effects. *Chem. Commun.* **2013**, *49*, 6340–6342. [[CrossRef](#)] [[PubMed](#)]
39. Dorbes, S.; Valade, L.; Real, J.A.; Faulmann, C. $[\text{Fe}(\text{sal}_2\text{-trien})][\text{Ni}(\text{dmit})_2]$: Towards switchable spin crossover molecular conductors. *Chem. Commun.* **2005**, 69–71. [[CrossRef](#)] [[PubMed](#)]
40. McPhillips, T.M.; McPhillips, S.E.; Chiu, H.J.; Cohen, A.E.; Deacon, A.M.; Ellis, P.J.; Garman, E.; Gonzalez, A.; Sauter, N.K.; Phizackerly, R.P.; et al. Blu-Ice and the distributed control system: Software for data acquisition and instrument control at macromolecular crystallography beamlines. *J. Synchrotron Radiat.* **2002**, *9*, 401–406. [[CrossRef](#)] [[PubMed](#)]
41. Cowieson, N.P.; Aragao, D.; Clift, M.; Ericsson, D.J.; Gee, C.; Harrop, S.J.; Mudie, N.; Panjikar, S.; Price, J.R.; Riboldi-Tunnicliffe, A.; et al. MX1: A bending-magnet crystallography beamline serving both chemical and macromolecular crystallography communities at the Australian Synchrotron. *J. Synchrotron Radiat.* **2015**, *22*, 187–190. [[CrossRef](#)] [[PubMed](#)]
42. Kabsch, W. XDS. *J. Appl. Crystallogr.* **1993**, *26*, 795–800. [[CrossRef](#)]
43. Bruker. SADABS, Version 2.11; Bruker AXS Inc.: Fitchburg, WI, USA, 2001.
44. Sheldrick, G.M. *SHELX-2014: Programs for Crystal Structure Analysis*; University of Göttingen: Göttingen, Germany, 2014.

45. Sheldrick, G.M. Crystal structure refinement with *SHELXL*. *Acta Crystallogr. Sect. C* **2015**, *71*, 3–8. [[CrossRef](#)] [[PubMed](#)]
46. Dolomanov, O.V.; Bourhis, L.J.; Gildea, R.J.; Howard, J.A.K.; Puschmann, H. *OLEX2*: A complete structure solution, refinement and analysis program. *J. Appl. Crystallogr.* **2009**, *42*, 339–341. [[CrossRef](#)]



© 2017 by the authors. Licensee MDPI, Basel, Switzerland. This article is an open access article distributed under the terms and conditions of the Creative Commons Attribution (CC BY) license (<http://creativecommons.org/licenses/by/4.0/>).